

**NuFact muon storage ring : study of a design based on solenoid focusing
decay straights**

G. Rees* and F. Méot†

April 14, 2006

Abstract

*RAL
†DAPNIA&LPSC

Contents

1	Introduction	3
2	Working hypothesis	3
3	Linear machine	3
3.1	Arcs	5
3.2	Solenoid straight	7
3.3	Tuning/Collimation/RF straight	8
3.4	Full ring	9
3.4.1	Beam envelopes	9
3.4.2	Closed orbits	10
3.4.3	Momentum dispersion (to be revisited)	10
3.5	Large amplitude motion, samples	11
4	Large amplitude tracking	12
4.1	3-D horizontal + $\delta p/p$ initial conditions	13
4.2	2-D vertical initial conditions	14
4.3	5-D $x - z - \delta p/p$ initial conditions	15
5	Transmission	16
5.1	$\epsilon_x = \epsilon_z = 3 \pi$ cm (norm.), $\delta p/p = \pm 1\%$	16
5.2	$\epsilon_x = \epsilon_z = 6 \pi$ cm (norm.), $\delta p/p = \pm 4\%$	17
	References	18

1 Introduction

The muon storage ring in the neutrino factory (NuFact in the following) is located at the high energy end of the muon acceleration chain. It delivers the μ^+/μ^- decay neutrinos to physics detectors.

The design of concern here, is a triangle geometry 20 GeV storage ring (upgradable to 50 GeV) (Fig. 1), parameters in Tab. 1, which features two decay straight sections, each one aiming at a distant detector. The third straight section of the ring is devoted to tuning, collimation and RF.

A particularity of the proposed design, is in its being based on solenoid focusing decay straights, a solution which has the advantage, compared to an equivalent quadrupole focusing system, to yield maximum betatron amplitudes about twice as small, hence saving on apertures.

The goal of the present work is to show the viability of this design, otherwise described in detail in Ref. [1], in particular as concerns the impact of the solenoid focusing on machine behavior. It addresses the questions of residual coupling, machine acceptance, and concludes with a computation of beam transmission over a few hundred turns.

2 Working hypothesis

A detailed description of the design principles and of the lattice can be found in Ref. [1]. Unless otherwise mentioned, working conditions, design parameters, etc., refer to it. The present study is based on stepwise ray-tracing [2], for the sake of accuracy in the representation of magnetic fields (combined function dipoles, solenoids, fringe fields, etc.), however two matrix optics codes are used in addition for building the ray-tracing data files, and for cross-checks, namely, BETA [3] and MAD [4].

The report is organized as follows :

Section 3 establishes the basic optical properties of the storage ring, on the basis of ray-tracing methods, with cross-checks using matrix codes, and establishes the accuracy of the thousand turns range multiturn stepwise ray-tracing. Section 4 describes the machine behavior in presence of largest amplitude motion. Transmission simulation results are given in Section 5.

Various Appendices give additional details concerning the optics, numerical data, methods.

3 Linear machine

Goals, methods

This preliminary Section 3 has various aims :

- ensure the correctness of the ray-tracing data and data files
- maximise the integration step sizes so to maximise the tracking speed while preserving high enough symplecticity over about 10^4 turns in the ring (which is more than one order of magnitude larger than the required storage).
- set up ray-tracing data that yield first order quantities : phase advances, betatron amplitudes, dispersions, etc., which stick as much as feasible to the matrix transport outputs. Ray-tracing cross-checks against matrix methods are done using MAD [4] and/or BETA [3] computer codes (in principle both yield identical results).

Various hypothesis concerning the tracking data

- In the muSR, most dipoles are combined function magnets. This raises the question of the respective values of the dipole field and of the radial magnet positioning. These quantities can be arbitrarily chosen with the sole constraint of yielding zero closed orbit and correct dispersion function. Therefore our hypothesis in the present work is the following : the bending strength $B_0/B\rho = 1/\rho$ is taken equal to that of the reference ring, namely from the early G. Rees data [1], the ensuing positioning is determined so to cancel the closed orbit.

Table 1 : Muon storage ring parameters.

The right column gives, where worth, the stepwise ray-tracing data.

		Matrix	Ray-tracing
Energy	(GeV)	20	
Circumference	(m)	1170.764	
Requested transverse acceptance	(π cm, norm.)	3	
Requested $\delta p/p$ acceptance	(%)	± 1	
ν_x/ν_z		10.79 / 11.15	10.791 / 11.147
ξ_x/ξ_z			-14.3 / -14.9
Arcs (Fig. 3)			
<i>Short arcs (2) :</i>			
Length	(m)	78	
Deviation	(deg)	96.73	
No. cells		10	
Phase advance (μ_x/μ_z)	(2π)	2 / 2	
<i>Long arc (1) :</i>			
Length	(m)	124.8	
Deviation	(deg)	154.766	
No. cells		16	
Phase advance (μ_x/μ_z)	(2π)	3.2 / 3.2	
<i>Arc cell :</i>			
Length	(m)	7.8	
Phase advance	(deg)	72	
$\beta_{x,z}$ max	m	12.6	
D_x max	m	1.08	
<i>Arc cell combined function dipole :</i>			
Length	(m)	1.25	
Deviation	(deg)	4.836	
Curvature	(1/m)	0.337647	
Foc. strength	(m^{-2})	± 0.16	
Production Straight (Fig. 5)			
Length	(m)	126	
Number of solenoids	(/straight)	8	
Solenoid field	(T)	4	
Phase advance (μ_x/μ_z)	(2π)	0.5 / 0.5	
$\beta_{x,z}$ max	(m)	100	
Tuning/Collimation/RF straight Straight (Fig. 7)			
Length	(m)	148.364	
Phase advance (μ_x/μ_z)	(2π)	1.62 / 2.05	
$\beta_{x/z}$ max	(m)	103 / 58	
D_x max	(m)	0.7	
Matching sections			
Phase advance (μ_x/μ_z)	(2π)	0.97 / 0.9	

The diagram shows a circular muon storage ring. On the left side, there is a vertical section labeled 'Tuning/Collimation/RF straight Straight (Fig. 7)'. Moving clockwise from the top, there are two 'Short arcs (2)', followed by a 'Long arc (1)'. The bottom of the ring is a 'Production Straight (Fig. 5)'. The right side of the ring is composed of 'Arcs (Fig. 3)' which include 'Arc cell' and 'Arc cell combined function dipole' sections. The ring is composed of various magnetic elements represented by small rectangles and circles along the path.

Figure 1: Muon storage ring. The Tuning/Collimation/RF is placed vertical, on the left. The 8-solenoid decay straights are the two others.

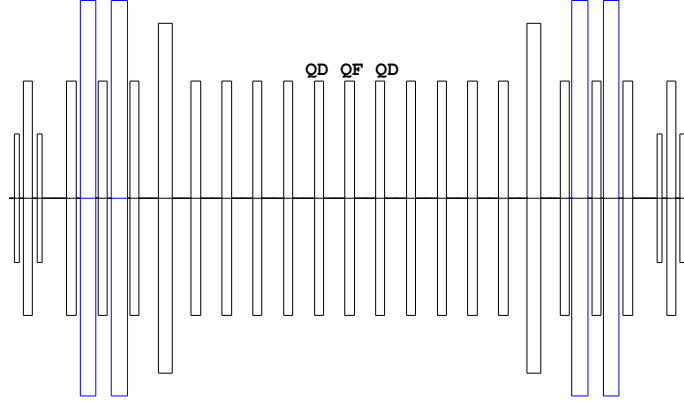


Figure 2: Tuning/Collimation/RF straight, comprised between the two 10-cell arcs. The section comprises 4 dipoles (blue), and quadrupoles with three different lengths. The four central cells ($\frac{1}{2}QF - QD - \frac{1}{2}QF$) are used for tune adjustment, adaptation to the - invariable - arc conditions is realized by buffer cells. The process requires a couple of iterations.

We leave to further inspection the question of the exact reference field and positioning of these magnets.

- In this process of dipole positioning, the quadrupole strengths (K_1) are to be slightly adjusted so to obtain phase advances values of Ref. [1].

- Bends are all sector in G. Rees hypothesis, they all are taken parallel face in Zgoubi. However, (i) this only has very little effect on K_1 , (ii) for various reasons, such as the presence of fringe fields, the phase advances of the ring pieces (arcs, decay straights, etc.) in the ray-tracing case need however be slightly readjusted so to identify with the matrix transport data ; this will take care of that sector/rectangular dipole consideration.

- Fringe fields are set in all dipoles, quadrupoles and solenoids, typical shapes are shown in Figs. 3, 5. However, in case of ray-tracing using sharp edge dipole field models (“no fringe fields”), vertical focusing is simulated by a first order kick, $\Delta z'/z = -\tan(w)/\rho + f/(6\rho^2 \cos(w))$, with $f=20$ cm, w = angle between the trajectory and the normal to the magnetic face, ρ = local curvature radius. This is necessary for getting any first order vertical focusing at all, since the “sharp edge” field model assumes $B_s \equiv 0, \forall s$.

Choice of tunes, adjustment

They should be kept away from 3rd to 5th order resonances. Alternate values to the present ones, 10.79/11.15 (Tab. 1), can be, 10.83/11.17, 10.62/11.38, or, furthest from 5th order resonance, 10.71/11.29. To be avoided, $\nu_x = 10.8, 10.6, \nu_x = 11.2, 11.4$.

Tune adjustments are realized using the two pairs of cells ($\frac{1}{2}QF - QD - \frac{1}{2}QF$) located on both sides of the tuning straight section central quadrupole, as schemed in Fig. 2.

3.1 Arcs

The arc cell has the form

$$[D8, BFA, D8, BDA]$$

optical functions are shown in Fig. 3. The arcs have the form

$$[BDE, N * (D8, BFA, D8, BDA), D8, BFA, D8, BDE]$$

Arc cell

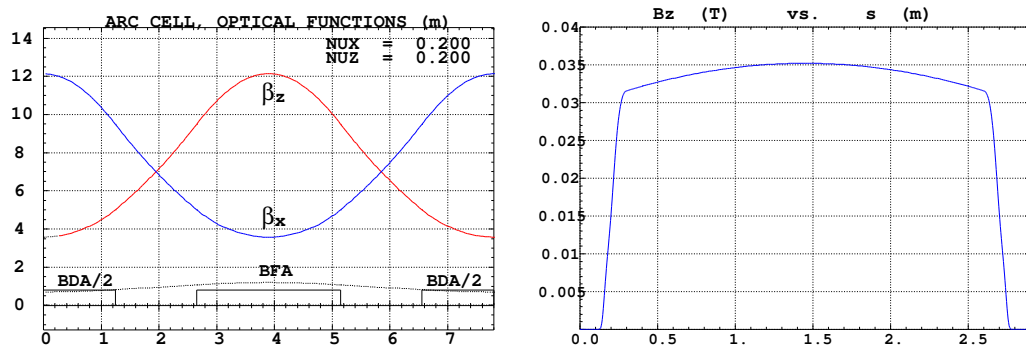


Figure 3: Left : arc cell, optical functions and periodic dispersion. Right : typical field at traversal of a combined function BFA-type dipole, including fringe fields, in the stepwise ray-tracing method.

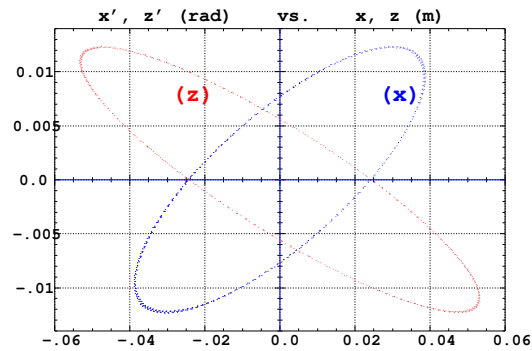


Figure 4: Horizontal and vertical phase space motion of a single particle, 10^5 passes, as observed at ends of arc cell. The particle has been launched on $\epsilon_x = \epsilon_z = 6 \pi \text{ cm}$ (norm.).

wherein $N = 9$ or $N = 15$ for respectively the two 10-cell and the single 16-cell arcs, $BDE = \frac{1}{2}BDA$, D8 is a 1.4 m drift, and with other characteristics as described below.

Table 1: Ray-tracing data concerning the arc cell, together with matrix method hypothesis for comparison.

Magnet		type	length (m)	$1/\rho$ (m^{-1})	K_1 (m^{-2})	angle (rad)	shift ($10^{-2}m$)
BFA	<i>Matrix method</i>	sbend	2.50	0.0337647	0.1580318	0.0844117	0
	<i>Ray-tracing</i>	sbend	2.50	id.	0.15917403	id.	1.78275
BDA	<i>Matrix method</i>	sbend	2.50	0.0337647	-0.1592295	0.0844117	0
	<i>Ray-tracing</i>	sbend	2.50	id.	-0.15817843	id.	1.72389
BDE	<i>Matrix method</i>	sbend	1.25	0.0337647	-0.1592295	0.0844117	0
	<i>Ray-tracing</i>	sbend	1.25	id.	-0.15817843	id.	0.4334

Satisfactory degree of symplecticity over 10^5 passes on the maximum invariant 6π cm in the cell is ensured using respectively 120/160/120 integration steps in the about 40 cm / 210 / 40 cm long entrance/body/exit regions of the BFA and BDA combined function dipoles. This is shown in Fig. 4. For comparison, taking 30/40/30 integration steps instead would yield horizontal phase space similar to that in Fig. 4, yet would entail noticeable smear in the vertical invariant.

3.2 Solenoid straight

The focal length in the solenoids satisfies

$$1/f_s == \int (B_s/2B\rho)^2 ds \approx L(B_s/2B\rho)^2$$

with L =length, B_s =longitudinal field.

The rotation of the decoupling-free frame is $\Omega = \int (B_s/2B\rho) ds \approx B_s L/2B\rho$

Characteristics of the solenoids in the two methods are as follows :

	length (m)	$B_s/2B\rho$ (m^{-1})	fall-off extent (m)	Ω (rad)
<i>Matrix method</i>	4	0.0318503	0	*** (a)
<i>Ray - tracing</i>	4	0.0331322	4	*** (b)

(a) Equation above.

(b) Assessed numerically.

Solenoid straight

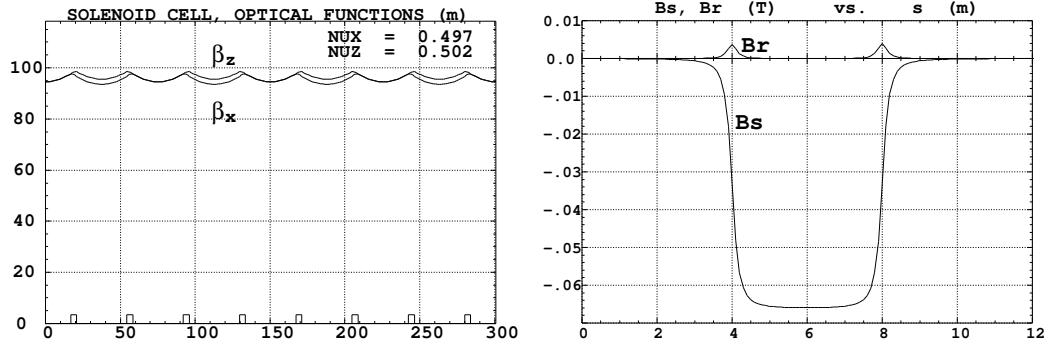


Figure 5: Left : optical functions in the solenoid straight. Right : typical field components at traversal of a solenoid, off-axis, in the stepwise ray-tracing model.

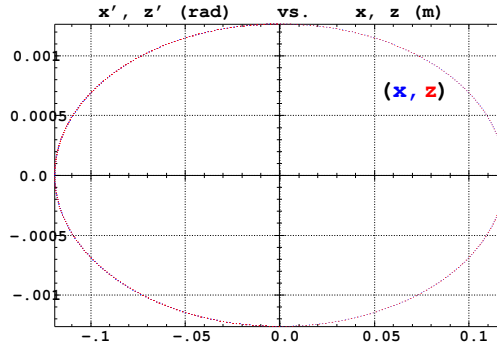


Figure 6: Horizontal and vertical (superimposed) phase space motion of a single particle, stepwise tracked over 2000 passes through the solenoid straight, observed at the straight end. The particle has been launched on $\epsilon_x/\pi = \epsilon_z/\pi = 3\pi\text{cm}$ invariants, the phase advance is $0.4976 \times 2\pi$ per pass. An ellipse fitting yields $\beta_x = \beta_z = 94.4\text{ m}$, $\alpha \approx 0$. The integration step size is 1 cm, the fringe field extent accounted for is 4 m at both ends of the solenoids.

3.3 Tuning/Collimation/RF straight

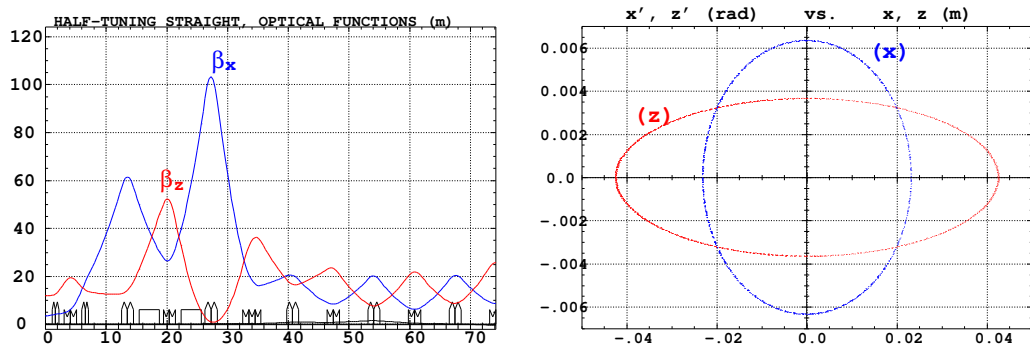


Figure 7: Left : optical functions in half the collimation/tuning/RF straight (from arc to straight center). Right : a 10^4 -pass tracking of a single particle launched with $\epsilon_x = \epsilon_z = 3\pi\text{ cm}$ (norm.), through the collimation straight ; x and z phase space motion are observed at the straight end ; this yields $\beta_x = 3.65\text{ m}$, $\beta_z = 11.60\text{ m}$, $\alpha_{x,z} \approx 0$; integration step size in quadrupole fringe field and body regions are respectively about 0.5 cm and 5 cm.

3.4 Full ring

The goal of this Section is, prior to further large amplitude and DA tracking, to show the correct behavior of the stepwise ray-tracing and multiturn tracking over the ring, in terms of first order invariants, envelopes, etc.

3.4.1 Beam envelopes

A set of 50 particles is launched, these particles are evenly spread on a $\epsilon/\pi = 3$ cm invariant, either pure (x, x') or pure (z, z') , while $\delta p/p \equiv 0$. This set is tracked for a single turn. This yields the excursions along the ring, i.e., with extreme excursions coinciding with the horizontal and vertical envelopes. Results are given in Fig. 8, together with envelopes obtained from matrix transport for comparison. It can be verified that the agreement is good.

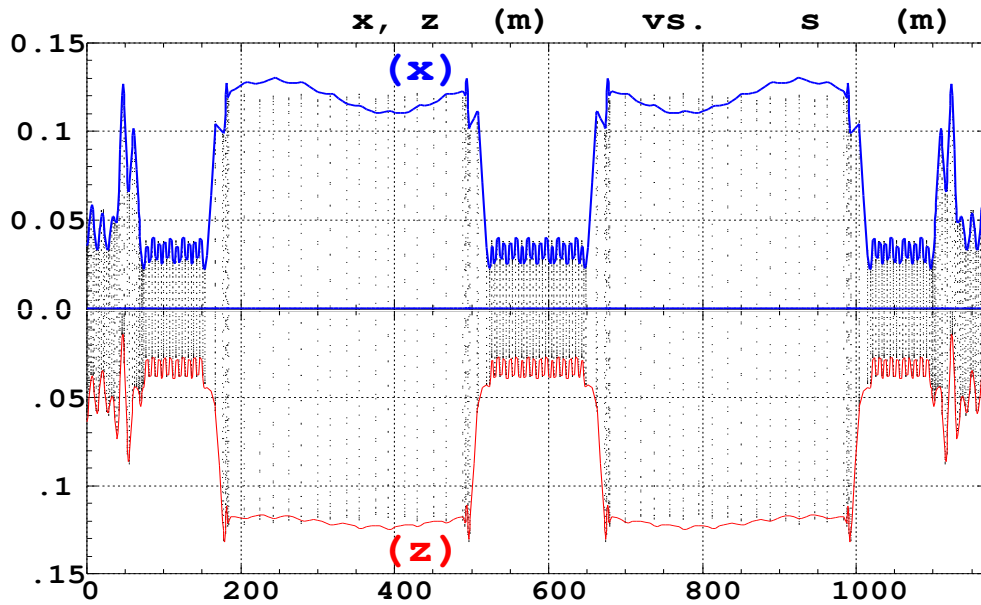


Figure 8: Transverse positions, inside all optical elements, of 50 particles starting with coordinates taken on $\beta\gamma\epsilon_{x,z} = 3\pi$ cm, together with the envelopes obtained from regular matrix computation for comparison (solid lines).

3.4.2 Closed orbits

The residual geometrical closed orbits, induced in the horizontal plane by the combined function dipoles and coupled into the vertical plane by the solenoids, are shown in Fig. 9. It can be seen that these are small, with maximum amplitude less than 0.04 mm in x and less than 0.07 mm in z .

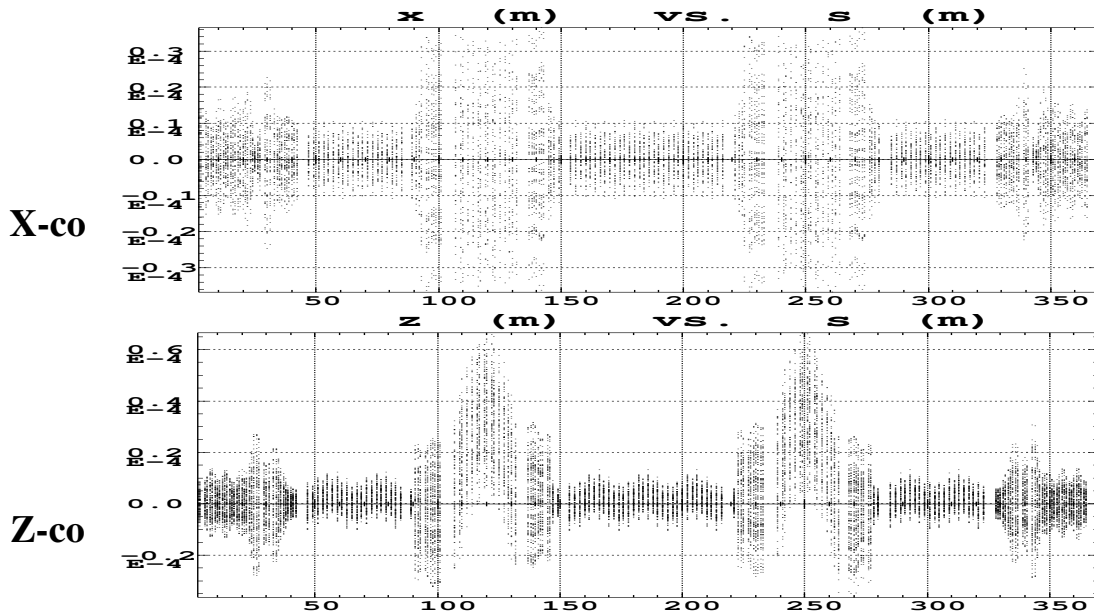


Figure 9: Residual geometrical closed orbits.

3.4.3 Momentum dispersion (to be revisited)

Dispersion functions are obtained by tracking the closed orbit of a chromatic particle, after normalization by $\delta p/p$. They are shown in Fig. 10, they reach maximum values $D_{x,max} \approx 1.1$ m, and, due to coupling $D_{z,max} \approx 1$ mm. It has been checked that the agreement with matrix methods is good.

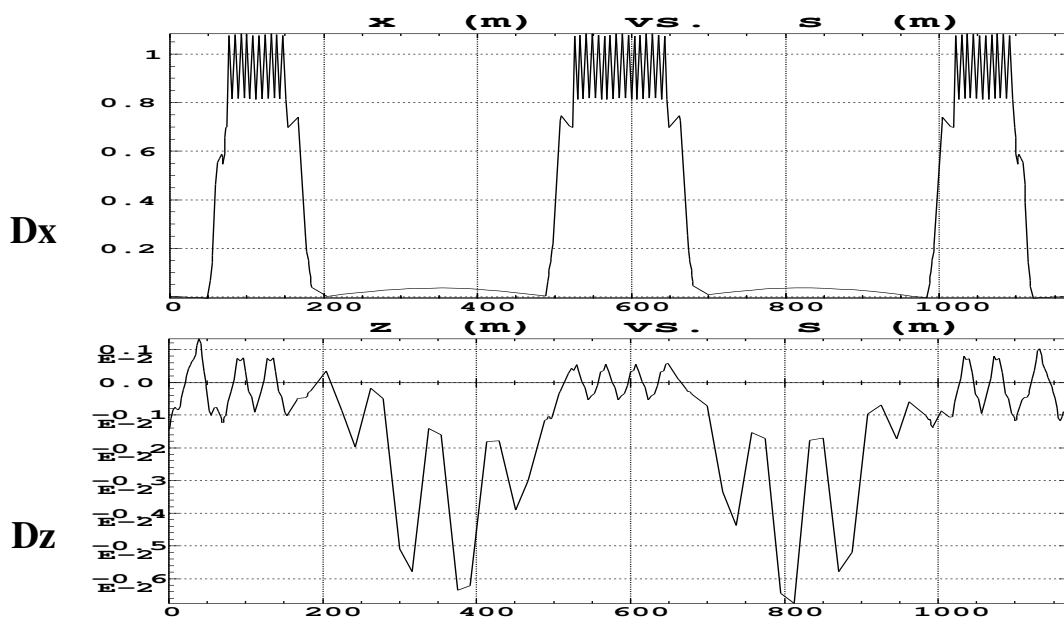


Figure 10: Chromatic closed orbits.

3.5 Large amplitude motion, samples

The results below have the mere goal of giving a rapid idea of expectable acceptances. They are clearly satisfactory and justify further inspection, next Sections.

In case of purely 2D initial beam coordiantes, multiturn stepwise ray-tracing yields the following maximum stable amplitudes :

Maximum stable starting invariant (normalized)	induced emittance	corresponding tunes ν_x/ν_z
$\epsilon_x/\pi = 2.64 \times 3 \pi \text{cm}$	$\epsilon_z/\pi = 0.01 \times 3 \pi \text{cm}$	0.799 / 0.182
$\epsilon_z/\pi = 2.63 \times 3 \pi \text{cm}$	$\epsilon_x/\pi = 0.03 \times 3 \pi \text{cm}$	0.825 / 0.155

If now non-zero $\delta p/p$ is introduced, the maximum stable amplitudes are sensibly decrease compared to the above, due to the absence of chromaticity corrections in the present optics. This is illustrated in Fig. 11 with $\delta p/p = 0.5\%$. The corresponding tunes are shown in Fig. 12, they differ from the $\delta p/p = 0$ ones ($\nu_x = 10.79, \nu_z = 11.15$, Tab. 1) by the amount $\Delta\nu_{x,z} = \xi_{x,z}\delta p/p$, with $\xi_{x,z} \approx -15$.

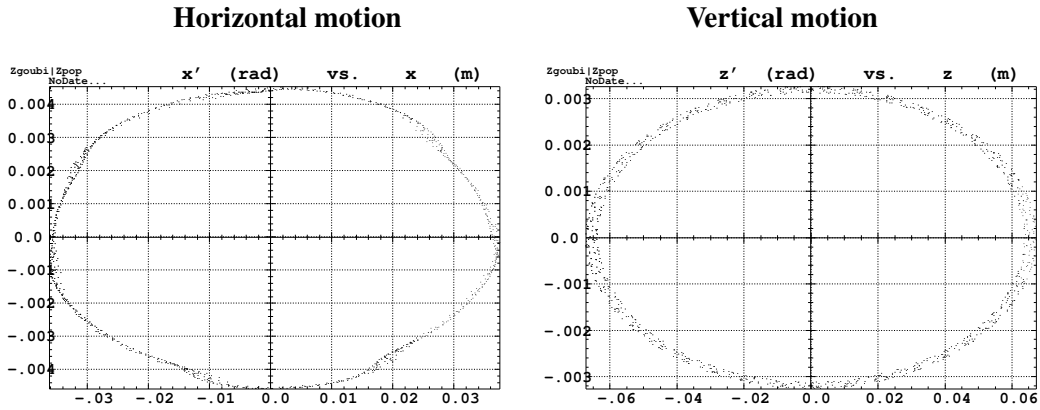


Figure 11: A particle launched on $\epsilon_x = \epsilon_z = 3.6 \pi \text{ cm}$ invariants and with $\delta p/p = 0.5\%$. 1000 turns in the ring.

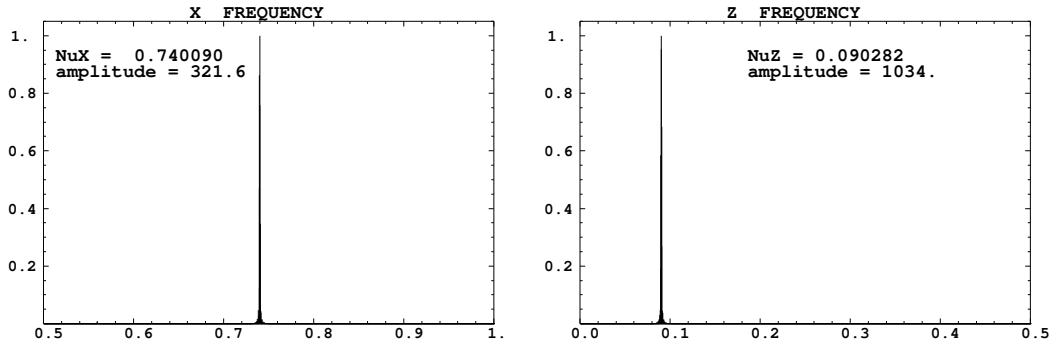


Figure 12: Corresponding spectra, victim of momentum detuning - natural chromaticities are about -15 in both planes.

4 Large amplitude tracking

Here, we first perform a series of test in order to control the large amplitude behavior, both of the tracking method, and of the ring itself. We limit the investigations in the $\epsilon_x/\pi = 3\pi\text{cm}$, $\epsilon_z/\pi = 3\pi\text{cm}$, $\delta p/p = \pm 1\%$ ranges, these will be pushed further in Section 5.2.

Initial conditions

Fig. 13 shows the initial distributions used in the following. They represent the beam at the middle of the tuning straight section.

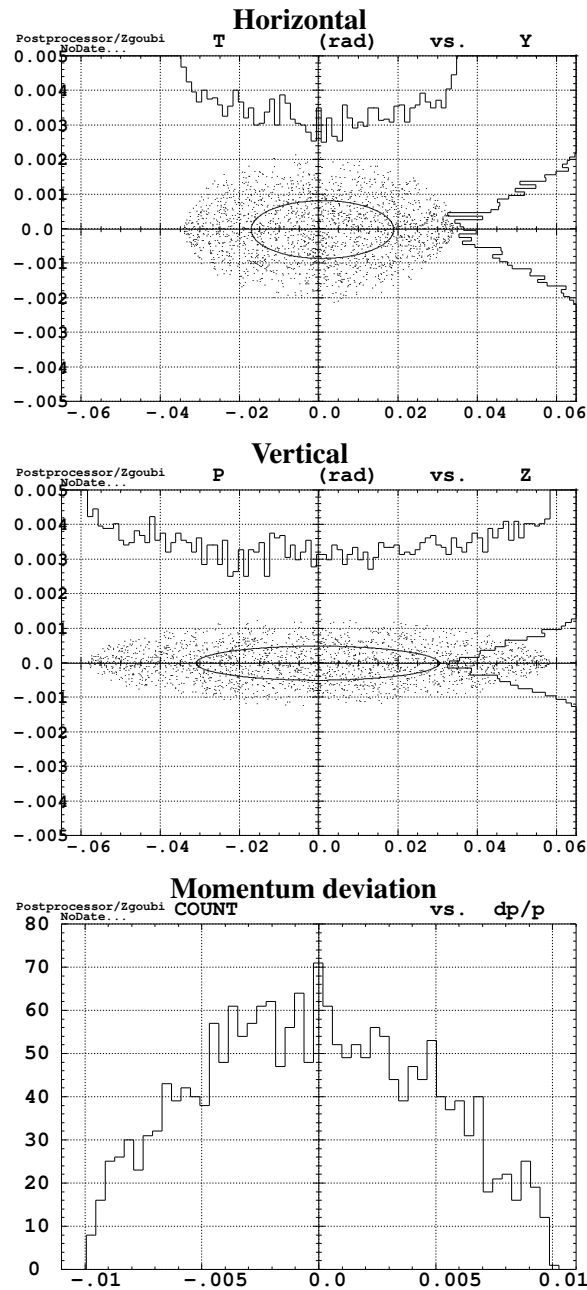


Figure 13: $\epsilon_x/\pi = 3\pi\text{cm}$, $\epsilon_z/\pi = 3\pi\text{cm}$, $\delta p/p = \pm 1\%$.

4.1 3-D horizontal + $\delta p/p$ initial conditions

An initial 200-particle beam with zero vertical initial amplitudes, initial (x, x') and $\delta p/p$ distributed as shown in Fig. 13, is tracked for a few hundred turns. The transmission is 100%. Fig. 14 shows the tracking results :

- the horizontal motion is strongly linear, up to the maximum emittance $\epsilon_x = 3\pi\text{cm}$,
- the coupling is very weak with the $\nu_x/\nu_z = 10.79/11.15$ on-momentum tune values, as a consequence the vertical motion induced is very small,
- corresponding Fourier spectra are shown in Figs. 14-(iii,iv), the vertical one is very weak, and shows a side peak due to the $x - z$ coupling,
- the beam extent in the tune diagram is mostly due to the chromaticities,
- in the amplitude-detuning plot in Fig. 14-vi, the ϵ_x/π value for each particle is drawn from *elliptical* fit of the particle motion in phase-space, which is justified, see Figs. 14-(i). The amplitude-detuning appears to be very weak, this is due to the absence of strong field non-linearities,

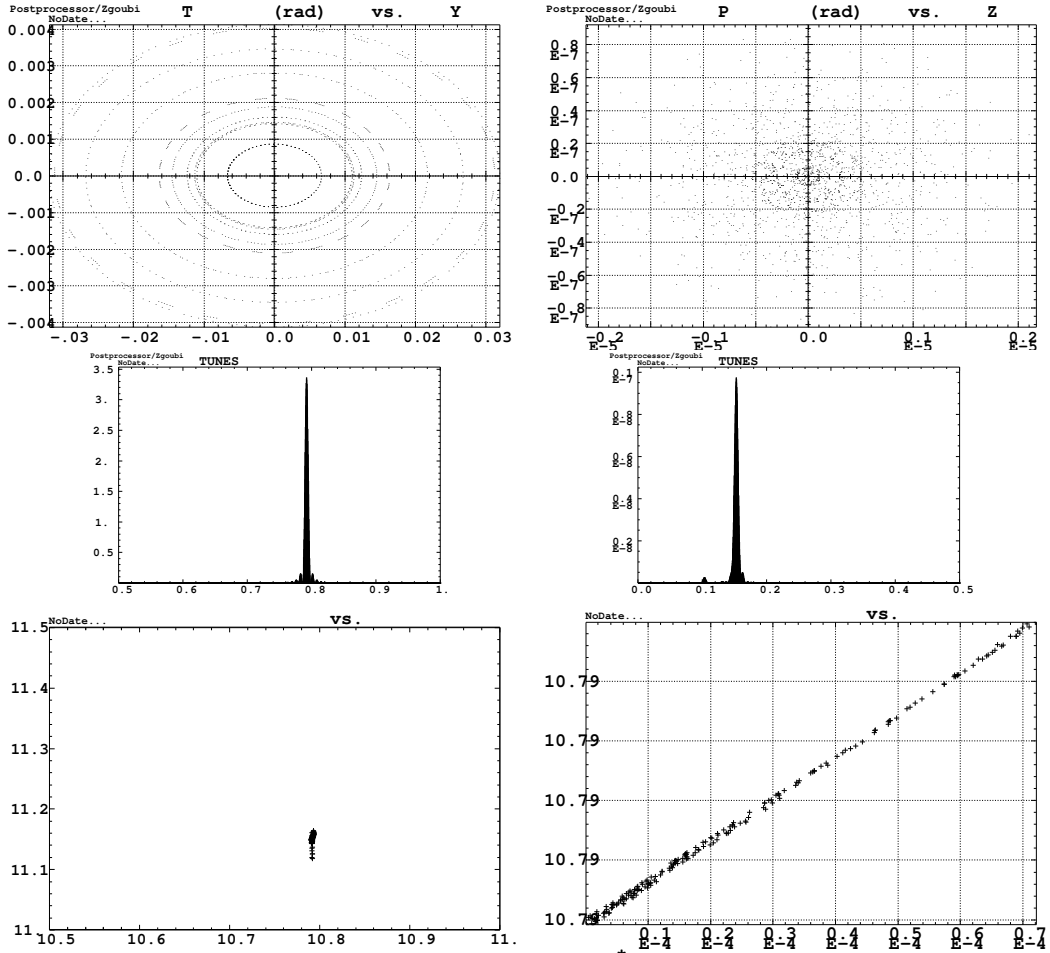


Figure 14: (i) Horizontal motion of sample particles, up to about 3π cm. (ii) Corresponding vertical motion, induced by coupling due to the solenoids. (iii, iv) Specimen ν_x and ν_z spectra. (v) Tune diagram for the 200 particles, obtained by Fourier analysis. (vi) Amplitude detuning, ν_x as a function of ϵ_x/π .

4.2 2-D vertical initial conditions

An initial 200-particle monoenergetic beam, with zero horizontal initial amplitudes, and with initial (z, z') distributed as shown in Fig. 13, $\epsilon_z = 3\pi\text{cm}$ (norm.), is tracked for a few hundred turns. The transmission is 100%. Fig. 15 shows the tracking results :

- the horizontal motion is strongly linear, up to the maximum emittance $\epsilon_x = 3\pi\text{cm}$,
- the coupling is very weak with the $\nu_x/\nu_z = 10.79/11.15$ on-momentum tune values, as a consequence the vertical motion induced is very small,
- corresponding Fourier spectra are shown in Figs. 14-(iii,iv), the vertical one is very weak, and shows a side peak due to the $x - z$ coupling,
- the beam extent in the tune diagram is mostly due to the chromaticities,
- in the amplitude-detuning plot in Fig. 14-vi, the ϵ_x/π value for each particle is drawn from *elliptical* fit of the particle motion in phase-space, which is justified, see Figs. 14-(i). The amplitude-detuning appears to be very weak, this is due to the absence of strong field non-linearities,

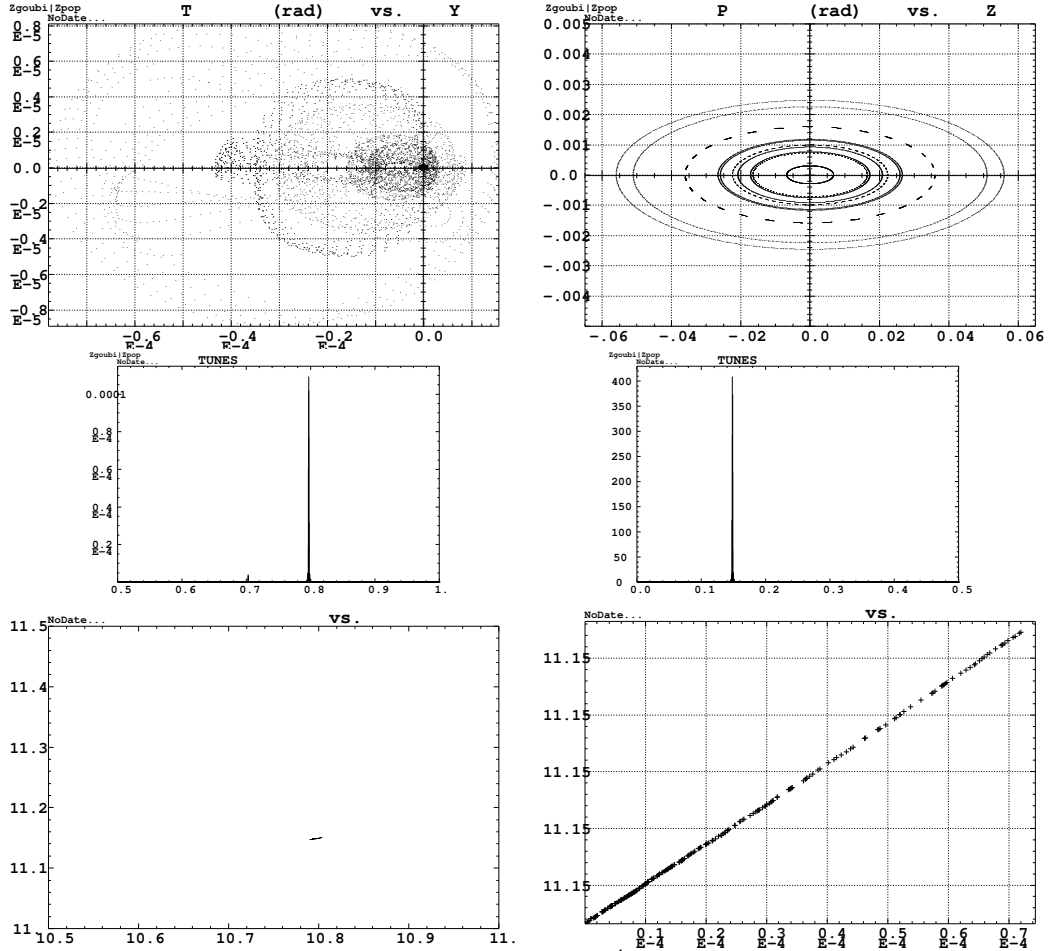


Figure 15: (i) Induced horizontal motion of sample particles, induced by coupling due to the solenoids. (ii) Vertical motion, up to about 3π cm. (iii, iv) Specimen ν_x and ν_z spectra. (v) Tune diagram for the 200 particles, obtained by Fourier analysis. (vi) Amplitude detuning, ν_z as a function of ϵ_z/π .

4.3 5-D $x - z - \delta p/p$ initial conditions

An initial 200-particle beam with initial $\epsilon_x = \epsilon_z = 3 \pi \text{cm}$ and $-1\% < \delta p/p < 1\%$, with distributions as shown in Fig. 13, is tracked for a few hundred turns. The transmission is close to 100%. Fig. 16 gives the tracking results.

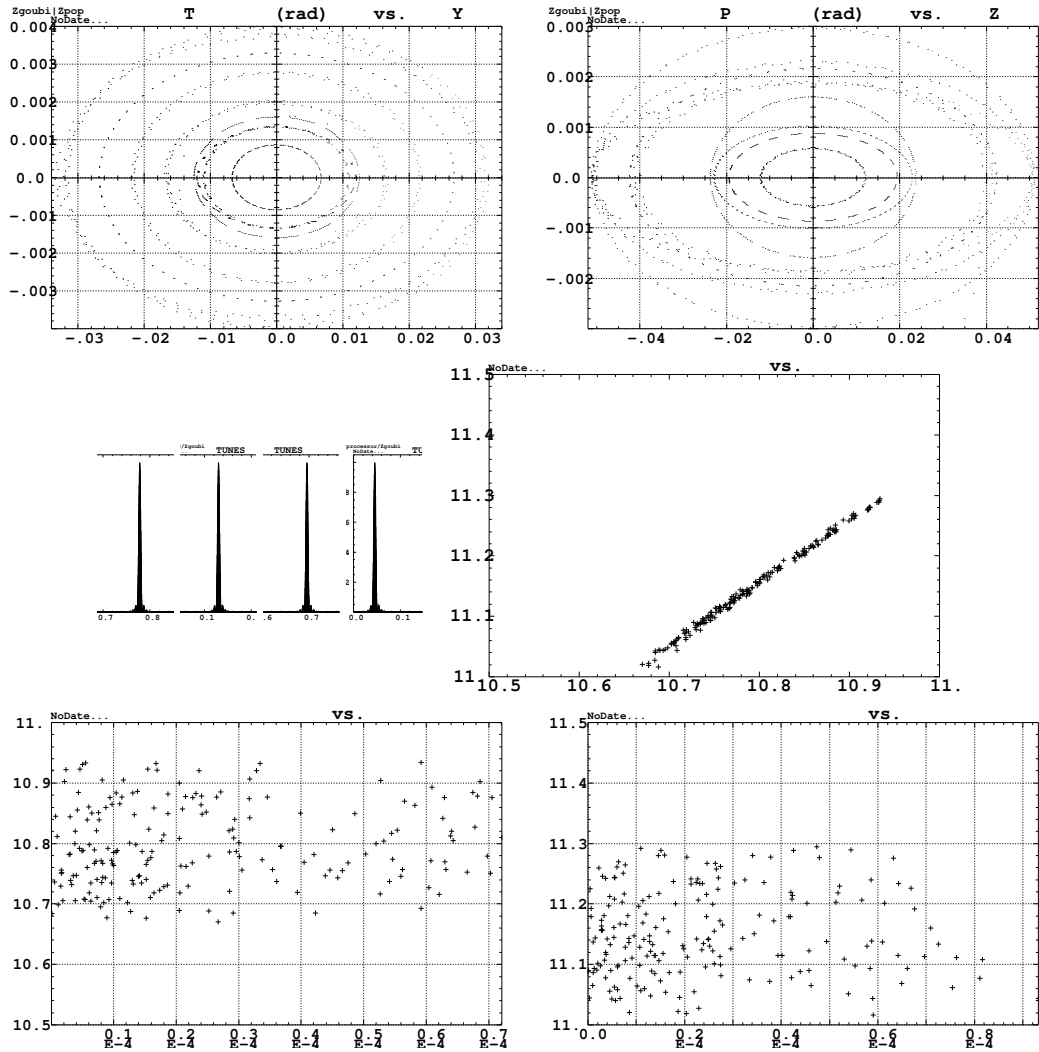


Figure 16: (i) Horizontal motion of sample particles. (ii) Vertical motion. (iii) Sample spectra, all with single peak, showing the negligible coupling. (iv) Tune diagram for the 200 particles, from Fourier analysis. (v) Amplitude detuning, horizontal, ν_x as a function of ϵ_x/π (drawn from elliptical fit of each particle motion in phase-space) (vi) Amplitude detuning, vertical, ν_z as a function of ϵ_z/π .

5 Transmission

5.1 $\epsilon_x = \epsilon_z = 3 \pi \text{ cm (norm.)}$, $\delta p/p = \pm 1\%$.

A 2000 particle beam is launched for 1000 turns around the ring. The initial conditions are those of Fig. 17, namely, total emittances $\epsilon_x = \epsilon_z = 3 \pi \text{ cm (norm.)}$, $\delta p/p = \pm 1\%$. The transmission is 1942/2000 particles. In other words, the acceptance of the defect-free ring, chromaticity non corrected, is larger than $3 \pi \text{ cm}$ transverse, $\pm 1\% \delta p/p$. The transmitted beam, after 1000 turns, is shown in Fig. 18, the momentum distribution (not shown) is unchanged. Fig. 20 shows the satisfactory behavior of the horizontal and vertical phase-space motions and of the numerical tracking.

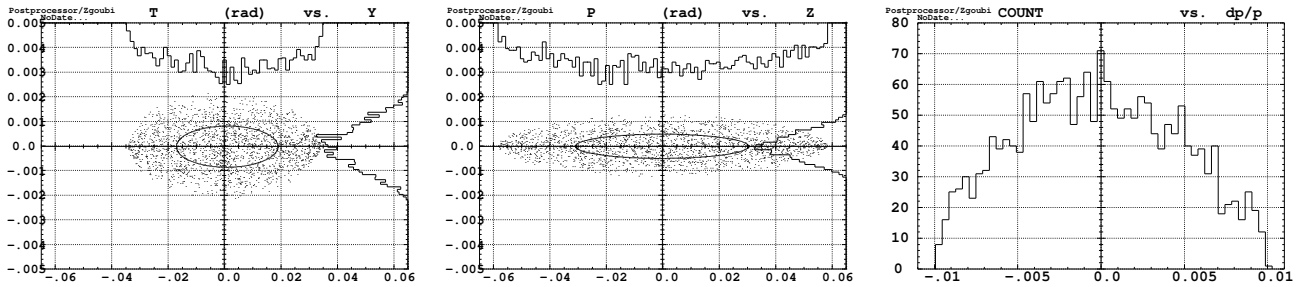


Figure 17: Initial conditions for transmission simulations. The local betatron functions are $\beta_x = 7.73 \text{ m}$, $\beta_z = 22.7 \text{ m}$, $\alpha_{x,z} = 0$, $D_{x,z} \approx 0$, $D'_{x,z} \approx 0$.

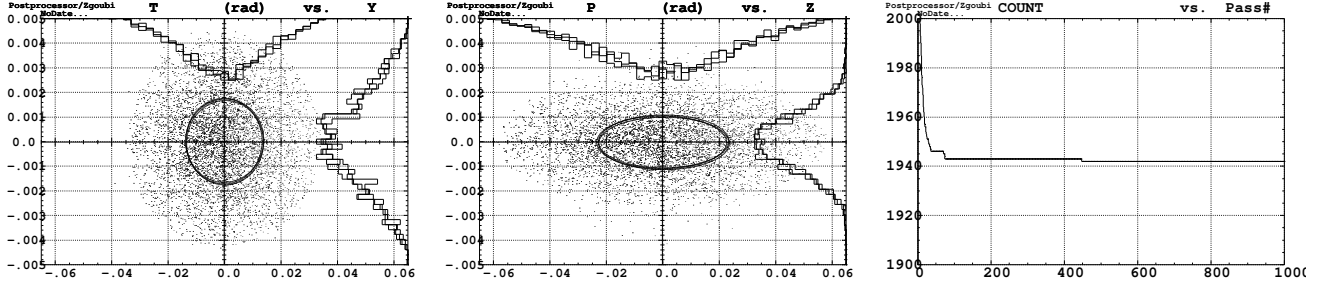


Figure 18: Left and middle : a superposition of (resp. H and V) phase spaces and projected densities at turns # 100, 500 and 1000 ; it can be observed that the emittance and densities practically do not change, meaning absence of sensible (numerical or real) diffusion effect. Right : number of particles transmitted vs turn number. Note : the apparent emittance increase, compared with Fig. 17, is the effect of momentum spread, in the absence of chromaticity corrections (adapted ellipse depends on $\delta p/p$).

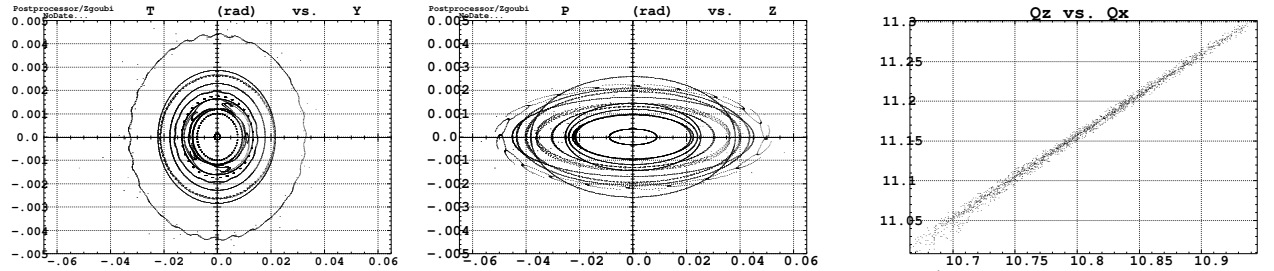


Figure 19: Sample multiturn tracking, some arbitrary particles with various H and V conditions. This shows the good behavior of the numerical integration (no evidence for non-symplectic behavior).

Figure 20: Beam footprint in the tune diagram, with extent due to the chromaticity.

5.2 $\epsilon_x = \epsilon_z = 6 \pi \text{ cm (norm.)}$, $\delta p/p = \pm 4\%$.

A 10^4 particle beam is launched for 1000 turns around the ring. The initial conditions are, total emittances $\epsilon_x = \epsilon_z = 6 \pi \text{ cm (norm.)}$, $\delta p/p = \pm 4\%$ (Fig. 21, blue curve). The transmission is 5500/10000 particles, transmission curve shown in Fig. 22-left, most of the losses occur during the first tens of turns, they are due to $\delta p/p$ induced resonant conditions. The transmitted beam, after 1000 turns, is shown in Fig. 22. It can be observed that, from Fig. 21 to Fig. 22, the (x, x') and (z, z') transverse densities change their initial parabolic shape to a final bell shape, this is due to the $d\beta_{x,z}/dp/p$ in the absence of chromaticity correction, which also result in an apparent emittance increase. Fig. 20 shows the satisfactory behavior of the horizontal and vertical phase-sspace motions and of the numerical tracking.

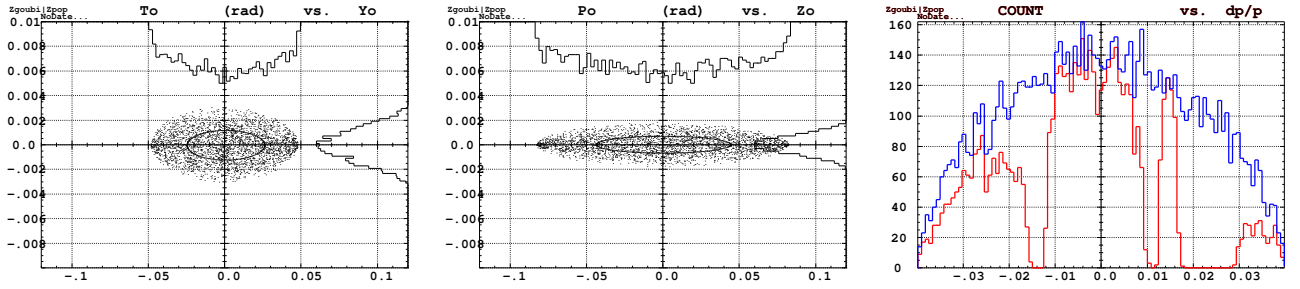


Figure 21: Initial conditions for transmission simulations, and transmitted momentum density (red histogram on the right). The local betatron functions are $\beta_x = 7.73 \text{ m}$, $\beta_z = 22.7 \text{ m}$, $\alpha_{x,z} = 0$, $D_{x,z} \approx 0$, $D'_{x,z} \approx 0$.

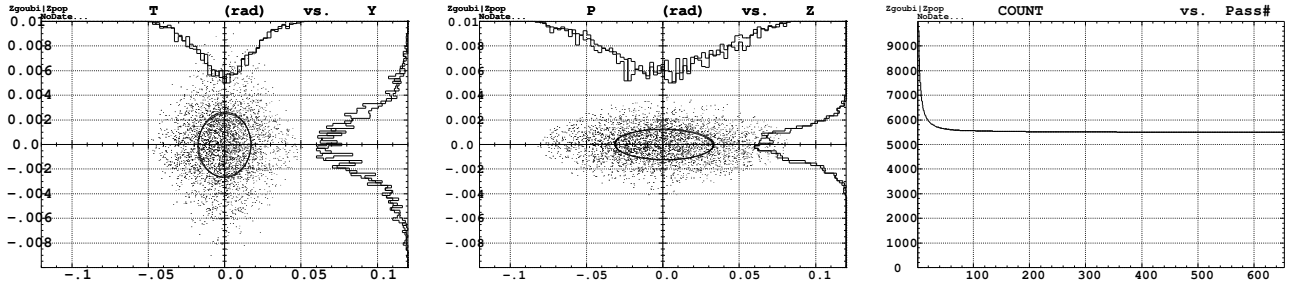


Figure 22: Left and middle : a superposition of (resp. H and V) phase spaces and projected densities at turns # 300 and 650 ; it can be observed that the emittance and densities practically do not change, meaning absence of sensible (numerical or real) diffusion effect. Right : number of particles transmitted vs turn number. Note : the apparent emittance increase, compared with Fig. 21, is the effect of momentum spread, in the absence of chromaticity corrections (adapted ellipse depends on $\delta p/p$).

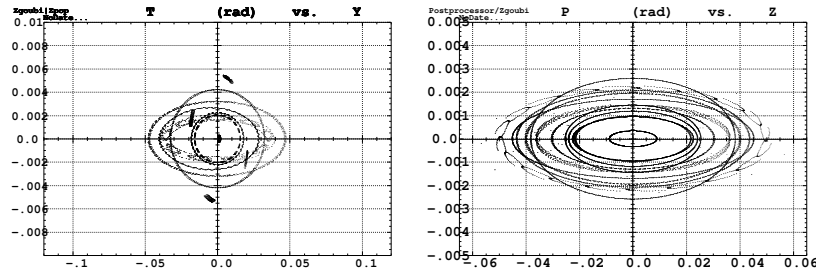


Figure 23: Sample multiturn tracking, height arbitrary particles with various H, V and $\delta p/p$ conditions. This shows the good behavior of the numerical integration (no evidence for prohibitive non-symplectic behavior).

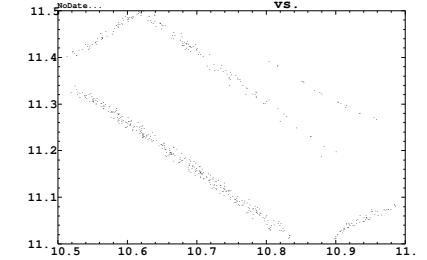


Figure 24: Beam footprint in the tune diagram, with extent due to chromaticity and coupling.

References

- [1] G. Rees, Stormu20 (20 GeV, μ^+ and μ^- , Isosceles Triangle, Storage Rings.), private communication, Jan. 2006.
- [2] F. Méot, The ray-tracing code Zgoubi, NIM A 427 (1999) 353-356.
- [3] The BETA code, J. Payet, F. Méot, et *als.*, CEA/DAPNIA, Saclay.
- [4] H. Grote, F. C. Iselin, The MAD Program, User's Reference Manual, CERN/SL/90-13 (AP) (Rev. 5), CERN, 29 April 1996.
- [5] F. Méot, On the effects of fringe fields in the LHC ring, Part. acc., 1996, Vol. 55, pp.[329-338]/83-92.
- [6] F. Méot, On the effects of fringe fields in the recycler ring, Report FERMILAB-TM-2016, April 15, 1997.
- [7] G. Leleux, Compléments sur la physique des accélérateurs, DEA de Physique et Technologie des Grands Instruments, rapport CEA/DSM/LNS/86-101, CEA, Saclay (1986).
- [8] H.A. Enge, Deflecting magnets, in *Focusing of charged particles*, volume 2, A. Septier ed., Academic Press, New-York and London (1967).
- [9] G. Leleux, Influence of quadrupole fringe fields on wave numbers, Tech. report 6-67/GL-FB, LAL, Orsay (2 Feb. 1967).